Preliminary study of CO_2 frost formation during cryogenic carbon capture using tomography analysis

Yuan Chen [a], David Cann [b], Jiabin Jia [a], Carolina Font-Palma [b],[*]

[a] School of Engineering, University of Edinburgh, EH9 3BF Edinburgh, UK
[b] Department of Engineering, University of Hull, HU6 7RX Hull, UK

ARTICLE INFO

ABSTRACT

Cryogenic carbon capture (CCC) is a potential technological solution to reduce CO_2 emissions and achieve the needed environmental targets. CCC provides a relatively compact solution to industries where more mature technologies would have difficulty scaling down economically. However, there is a lack of research on frost formation of CO_2 within packed bed systems, despite the influence of the CO_2 frost layer on thermal conductivity leading to excessive cooling costs. Understanding the rate of CO_2 frost growth and accumulation within a packed bed is critical to the design of the capture column. Therefore, real-time quantitative imaging becomes increasingly desirable to study the CO_2 frost formation during cryogenic carbon capture, but it may be difficult by most of the traditional measurement methods. This study aims to investigate the use of an Electrical Capacitance Tomography (ECT) to monitor the real-time CO_2 frost formation in a fixed packed bed. In this work, the evolution of the permittivity distribution during the capture process has been investigated in detail by experiments, elucidating the effect of the bed material type and bed material temperature. An ECT sensor was constructed to measure frost distribution to elucidate the mechanisms of CO_2 frost formation by first testing on ice frost in the packed bed. The ECT images of ice formation were reconstructed by measurement data with a conventional algorithm. The results show that ECT could effectively monitor the changes of relative permittivity caused by the frost formation in real-time. With the help of an image reconstruction algorithm, the outline and position of the permittivity change area can be monitored. These results indicate that ECT has the potential to be a novel technique for monitoring CO_2 frost formation during cryogenic carbon capture.

1. Introduction

As the world's total energy consumption is projected to increase around 25 % in the Business-as-usual (BAU) scenario [1], where excessive emissions of CO_2 accelerates climate change [2]. Scientific evidence suggests that one of the dominant causes of climate change is the release of greenhouse gases (e.g., CO_2) [3]. The ambitious target of net zero-carbon emissions by 2050, agreed by the UK and other countries, has now made carbon capture and storage (CCS) a necessity. Carbon capture has focused on mature technologies, such as chemical absorption using amine-based solvents that require significant thermal energy for solvent regeneration. Post-combustion CO_2 capture is the preferred method for reducing CO_2 emissions [4], wherein the CO_2 being emitted by industries using fossil fuels is captured and either sequestered or used to generate a useful product [5]. The most common technology for post-combustion CO_2 capture uses chemical solvents;

however, current technologies are too energetically intensive for widespread adoption, and emerging lower energy options will require more development and demonstration under realistic conditions [6]. For large emitters, other methods of post-combustion carbon capture are more appropriate [7]. In previous studies on factors affecting post-combustion carbon capture absorption efficiency, experimental studies or pilot tests with column inner diameters from 19 mm to 597 mm with different types of packing have been summarized [8]. New technologies are emerging to overcome this shortcoming including membranes, calcium looping, direct air capture, cryogenic separation and liquefaction, but most face different technological challenges [9].

There is growing interest in cryogenic carbon capture (CCC) to address the need for new methods to capture carbon dioxide to tackle the current climate change crisis [10]. This method does not require chemicals, is capable of high CO_2 removal levels and delivery of a high purity of CO_2, which could be utilized in the food industry or to produce

chemicals. In general, the cryogenic process involves very low temperatures (around −100ºC or below) that freezes CO_2 on the surface. Previous studies on energy minimization in cryogenic packed beds during purification of natural gas with high CO_2 content has been carried out by Ali et al. [11], who investigated the effects of process parameters like initial temperature of the cryogenic bed, feed composition, and feed flow rate on energy requirement, bed saturation, bed pressure, and cycling times. Modelling work has been carried out to aid the prediction of carbon dioxide frost points of natural gas in LNG systems [12]. Further studies have found that the formation of the CO_2 frost and ice layer on the surface of a heat exchanger cause a decrease in the heat transfer rate and thus a decrease in process efficiency [13,14]. Those studies recognized the need for advanced configurations using packed beds that require periodic switching between CO_2 capture, sublimation and bed cooling conditions, by using several parallel beds [15]. Another configuration overcomes this limitation by using a moving cold packed bed, the advanced cryogenic carbon capture (A3C) process, which feasibility has been assessed through modelling and economic analyses [16]. The moving bed configuration allows frosted bed material to be regenerated in a continuous stage and be then recycled back into the capture column. Furthermore, the velocity of CO_2 frost advance within a static packed bed has been measured to support the design of a moving bed column to achieve continuous CO_2 removal [17].

The factors that affect overall CO_2 removal quality and efficiency in CCC systems are, therefore, the initial bed temperature, inlet CO_2 fractions, packing material and the frost layer produced on the surface of packing material [18]. Research concerning crystal (or nucleation) and frost growth is mostly related to water in moist air or refrigeration cycles. The one report available regarding binary data of nitrogen and CO_2 mixtures for the variation of frost thickness, density and thermal conductivity in a cryogenic plate used visual observations and photographs through the transparent packed column pipe [19]. However, visual observations and photographs can only provide information of the frost layer at the outer circle of the packed column and the overall volume fraction of frost cannot be directly calculated.

Thus, this study addresses this research gap through the application of a visualisation tool – Electrical Capacitance Tomography (ECT) to better understand CO_2 frost formation under varying factors. ECT has previously shown great potential for imaging and quantifies gas–liquid two-phase carbon dioxide flow in various CO_2 capture process applications [20,21]. This technique was earlier used for monitoring the distribution of co-current and counter-current flow in the packed column using tomography for liquid gas interactions for carbon capture using chemical absorption [22]. Recent studies [22,23] have shown an ECT system able to measure the liquid distribution of the liquid hold-up inside the packed column, whilst Xia et al. [24] used an electrical capacitance volume tomography to image LN_2-VN_2 phase distribution. Previous studies have confirmed the effectiveness of ECT sensors for large-scale applications. For example, Isaksen et al. [25] have attempted an ECT of 1 m diameter to measure multi-interfaces in an oil separator, and Wang and Yang [26] scaled up and tested successfully a 12-electrode ECT sensor of nearly 1 m diameter on a pharmaceutical fluidized bed. However, ECT has never been used to withstand extremely low-temperature conditions used in desublimation processes as studied in this research.

In this research, the imaging techniques of ECT is applied to monitor the grow of frost by the cryogenic carbon capture progress in a packed bed. An eight-electrode ECT sensor was constructed and a high-performance digital ECT system was used. The work aims to identify if there is dependence of ECT capacitance on the measured material composition (relative permittivity) and other operation conditions (e.g., temperature) used for cryogenic carbon capture, which should make possible the monitoring of CO_2 frosting progress and quantify the CO_2 frost by ECT using suitable algorithms. This study will enable a better understanding of the behaviour of CO_2 frost formation from a mixture of gases during controlled experiments in a packed column. To our best

knowledge, this is the first investigation of the CO_2 frost formation during cryogenic carbon capture using ECT.

2. Materials and methodology

2.1. Principle of electrical capacitance tomography (ECT)

ECT measures capacitances of materials between all electrode pairs. The measured data together with a pre-calculated sensitivity map are computed to estimate the cross-sectional permittivity changes within the sensing area. ECT estimates the internal permittivity distribution of the sensing area through boundary measurements. The mathematical theory of ECT is composed of two parts: the forward problem and the inverse problem. The forward problem corresponds to the calculation of the electrical capacitance on the electrodes from a known voltage and the relative permittivity distribution. For the forward problem, the linearized model describing the relationship between normalized capacitance data C_{norm} and the normalized permittivity change g is expressed as:

$$g = S^{-1}C_{norm} \tag{1}$$

where S is the sensitivity distribution matrix of normalized capacitance with respect to normalized permittivity, giving a sensitivity map for each electrode pair. The inverse problem corresponds to the calculation of the relative permittivity distribution from the known voltage and measured capacitance. Common image reconstruction algorithms were reviewed in reference [27].

The two methods used for calibration are described below. Two end calibration method: The ECT was calibrated between the lowest and the highest permittivity limits so that the intermediate pre-pixel normalized capacitance change at each measurement projection during the cryogenic carbon capture gas–solid conditions is expressed as.

$$C_{norm} = \frac{C_{mea(j)} - C_{l(j)}}{C_{H(j)} - C_{l(j)}}, j = 1, 2, \cdots, N \tag{2}$$

where j is the location of the measurement projection, N represents the total number of measurements. $C_{mea(j)}$ is the measured capacitance at the jth location. $C_{l(j)}$ and $C_{H(j)}$ are the reference capacitance at the jth location when the sensitive field is full of low permittivity media (e.g. CO_2 gas) and high permittivity media (e.g. CO_2 ice) respectively.

Single end calibration method: In cryogenic carbon capture applications, the high calibration with high permittivity media $C_{H(j)}$ is inconvenient to acquire as it would require the column cross section to be filled with CO_2 ice. A normalization method with single reference media can also be used in this work in order to expand the ECT's application [22]. The normalization model is expressed in Eq. (3):

$$C_{norm} = \frac{C_{mea(j)}}{C_{ref(j)}}, j = 1, 2, \cdots, N \tag{3}$$

where $C_{ref(j)}$ is the reference capacitance when the packed column is full of low permittivity media.

The absent of high calibration could have a detrimental effect on the accuracy of the results. To compare the results with and without high calibration, the root mean square (RMS) error, E_{RMS} under the single end calibration condition is evaluated from the following equation:

$$E_{RMS} = \left(\frac{\sum_{i=1}^{M-1}\sum_{j=i+1}^{M}\left(C_{norm(i,j)} - 1\right)^2}{\frac{M(M-1)}{2}} \right)^{\frac{1}{2}} \tag{4}$$

where M is the number of electrodes, $C_{norm(i,j)}$ is the normalized capacitance of the electrode pair $i-j$.

2.2. Experimental set up

The capture column test rig consists of a small-scale cryogenic

carbon capture application as shown in Fig. 1, located at the University of Chester and more details can be found in [17]. The experimental rig is made from a PTFE pipe, the internal and external diameters of the column are 72 mm and 95 mm, approximately 1 m in height. Two feed gas injector pipes feed into the capture column, i.e. a vertical cooling gas injector and a horizontal mixed gas injector. The gas injector pipes are made from copper pipes with a series of 1 mm width perforations across the length of the pipe that is located inside the column, on opposite sides of the copper pipe to allow gas to flow into the column uniformly. The ECT sensor electrodes were located approximately 120 mm from the bottom of the column. The capture column was tested using small ceramic beads of Zirconia partially stabilized with Yttria from Chemco Advance Material Co., ltd., ranging between 1.4 and 1.7 mm in diameter. The temperature of the bed material is recorded using thermocouples and data loggers. The thermocouples are inserted into the capture column from the top of the column and are adjusted to an appropriate height above the horizontal mixed gas (-60 ℃) injector.

Nitrogen and CO_2 for the gas streams are supplied by BOC cylinders, with purities of 99.98 % and 99.8 %, respectively. The two gas injectors are used for the cooling step and capture step. The vertical cooling gas injector feeds nitrogen gas that is first cooled to -140 ℃ by passing through the liquid nitrogen bath, which cools down the ceramic bed material. The horizontal mixed gas injector feeds in a mixture of nitrogen and CO_2 gas. The mixed gas is controlled by two automatic Bronkhorst El-Flow mass flow controllers, which set the flow rates for CO_2 and nitrogen gas before mixing the two gas streams together. The mass flow controllers provide a mixed gas flow at a specific CO_2 concentration v/v. The mixed gas is partially cooled by passing through a liquid nitrogen bath and further cooled by the bed material in the capture column. When the mixed gas is sufficiently cooled, the CO_2 present in the gas phase will desublime out of the gas phase and onto the bed material as a frost.

The composition of the mixed gas before entering the capture column and after leaving the capture column are measured with GSS CO_2 gas sensors, which have a precision of 0.001 %. The sensor in line before the capture column can detect between 0 and 20 % vol. CO_2 and the gas sensor in place at the outlet of the capture column can detect between 0 and 5 % vol. CO_2.

2.3. ECT sensor for cryogenic tomography

An ECT sensor with eight electrodes is designed in this study. Fig. 2 (a) shows the schematic illustration of the sensor. The sensors are made of copper foil. Eight electrodes of 6 cm length are mounted outside cryogenic packed beds and enclosed by an earthed guard electrode. Fig. 2 (b) illustrates the picture of the manufactured sensor equipped with a bubble wrap for insulating operation and shield electrode.

Fig. 3 illustrates the ECT system used in this work, and includes sensors, a data acquisition system and a computer with imaging software. The excitation signal is a sine wave with 14 Vp-p and 200 k Hz frequency. The ECT sensor is composed of 8 electrodes, providing a total of 28 independent capacitance measurements. The second component of the ECT system is a data acquisition system, which is a control circuit that allows all acquired signals are conditioned by the C/V circuit and transmitted to the computer through the USB [28]. The maximum signal-to-noise ratio (SNR) is 76.73 dB, and the minimum SNR is 62.25 dB among all the channels [22]. For image reconstruction purposes, the effect of random noise and system noise is mitigated by using averaged and normalized capacitance, which can be obtained from the single end or two end calibration. The data collected by the proposed measurement system can be used for real-time imaging at a frame rate of 714 fps.

2.4. Experimental campaign

The experimental procedure begins with an empty air-filled pipe ECT reference calibration measurement to check if all electrodes work normally. Next, the dry ceramic beads are added into the column and a second ECT measurement is made to determine calibration with dry ceramic beads. The position of thermocouples is adjusted based on ECT images. The temperature profiles from the thermocouples placed above and below the ECT were used to estimate the temperature of the bed material within the region of the ECT sensor.

For CO_2 frost experiments, the cooling stage delivered nitrogen gas at -140 ℃ to the bed material. When the bed material reached the desired

(a) Photo of experimental test rig
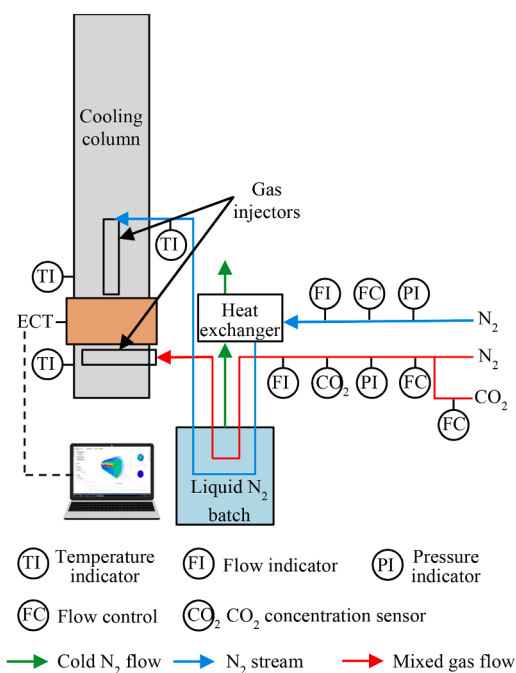
(b) Schematic diagram

Fig. 1. Pilot scale fixed bed experimental flow loop.
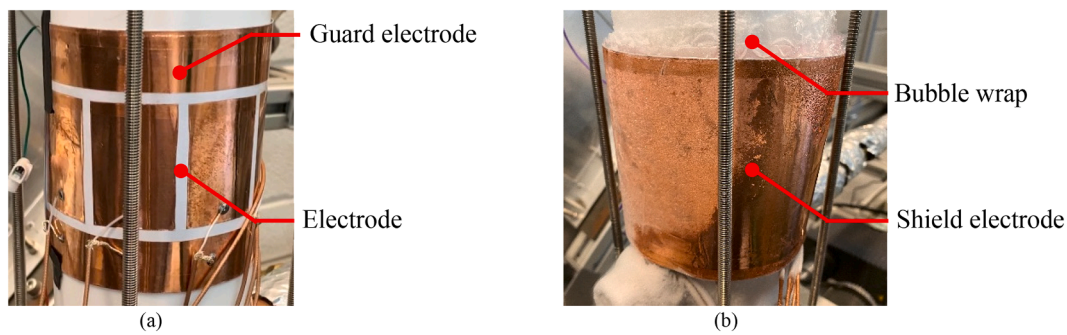
Fig. 2. Picture of (a) the manufactured ECT sensors with guard electrode and (b) bubble wrap with shield electrode.
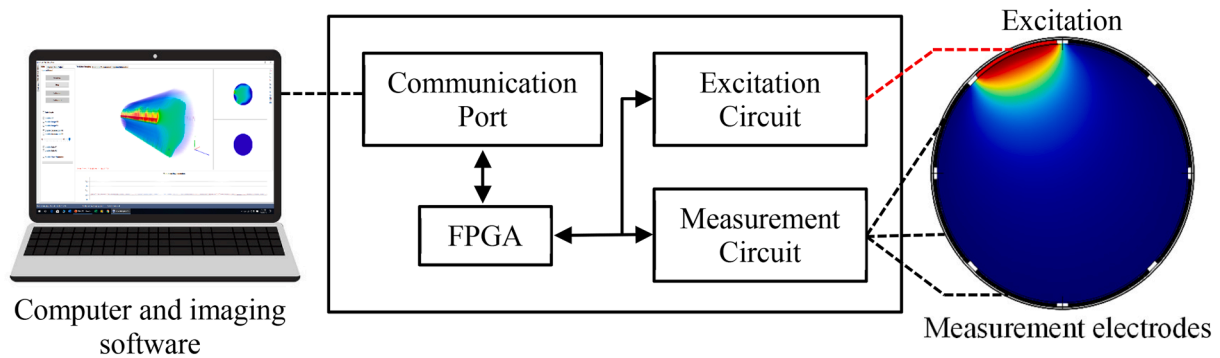
Fig. 3. Measurement principle of ECT.

temperature of roughly −120 ºC, the cooling stage was ended by shutting off the cooling gas stream. The ECT measurement procedure began when a cold ceramic-filled pipe ECT reference calibration measurement was taken for the ceramic packing with low permittivity material $C_{l(j)}$. The capture stage started by feeding a mixture of CO_2 and nitrogen through the mixed gas injector. The mixed gas, fed into the column at 40 L per minute (LPM) with 18 % CO_2 v/v, is partially cooled by passing through a liquid nitrogen bath to reach roughly –70 ºC. Heat transfer between the bed and the mixed gas within the capture column would then provide sufficient cooling to the mixed gas to cause CO_2 to desublime out of the gas phase as a frost and deposit onto the bed material.

The temperature profiles would be expected to show an increase in temperature and plateau at the desublimation temperature of CO_2, for a gas of 18 % CO_2 v/v, the desublimation temperature would be −97.2 ºC (estimated using the Span and Wagner equation of state [29]). The presence of this plateau in the temperature profiles identifies that CO_2 frost is forming within the bed and has reached equilibrium. As mixed gas continues to pass through the column, the temperature plateau will destabilise due to CO_2 defrosting at a faster rate than it is desubliming. Using the thermocouples above and below the ECT sensor helped to estimate when frost formation would be occurring within the region of bed material that the ECT sensor was measuring. When CO_2 starts defrosting, a second ECT measurement is made to determine ceramic packing with high permittivity material $C_{H(j)}$. Finally, after these two calibration references are taken, the ECT is connected to a computer where visualisation of the real-time images can be accessed on the computer screen, to determine whether the ECT sensor is able to detect frost formation. Also, ECT measurements were used to off-line reconstruct the permittivity distribution using the calculation method introduced in Section 2.1.

3. Results and discussion

3.1. CO₂ frosting experiment

Fig. 4 shows that ECT profiles at different bed temperatures do not change much, particularly at lower capacitance values. A small relative change of capacitance indicates that the relative change of permittivity is small, which means the relative permittivity change caused by CO_2 frost was insufficient to be detectable by the ECT sensor. A greater relative change of capacitance means that the change of actual size and position of the relative permittivity differ from the original value, thus
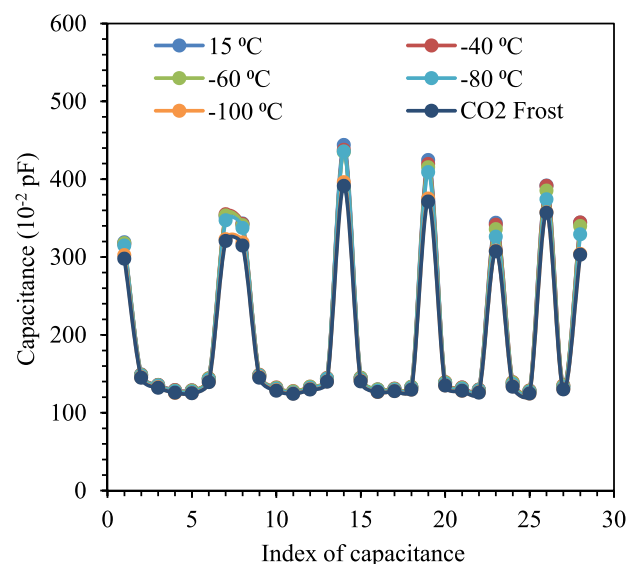
Fig. 4. ECT profiles for ceramic bed versus different temperature.

the reconstructed image can be a good presentation of the CO_2 frost change.

The temperature profiles in Fig. 5 show that the temperature below the ECT reached a plateau at approximately 150 s. The presence of the temperature plateau shows that indeed CO_2 frost is forming on the bed material.

As shown in Fig. 5, the capture step was started at roughly 80 s and the thermocouple below the ECT records a temperature profile roughly 70 s into the capture step. The plateau destabilises after 400 s as the temperature starts to rise again, indicating that the bed material is beginning to defrost. These results are consistent with data obtained in experimental analysis of CO_2 frost front behaviour studies [17]. According to Tuinier et al. [15], deposition of CO_2 causes a rise in bed temperature to an equilibrium value of approximately -93 °C and CO_2 breaks through after approximately 200 s. In our study, the equilibrium of approximately -92.8 °C was obtained by thermocouple above the ECT and CO_2 breaks through after approximately 130 s. The temperature profile for the thermocouple above the ECT did not demonstrate a plateau, which makes uncertain how fast frost accumulated in the capture column. Comparison with the ECT sensor readings during the CO_2 capture step is less accurate as a result.

Frost front velocity cannot be accurately predicted experimentally as the temperature profile above the ECT did not form a stable plateau. However, simulated predictions can be made for this experimental work and compared with simulated predictions using experimental results from Tuinier et al. [14] using correction factors derived in [17]. The correction factors consider the differences between flow rates, column dimensions, and bed material between the experimental set-ups, using equation 5 provided again below:

$$\frac{dv dy}{dc_p d\rho} \tag{5}$$

where y represents the volume fraction of CO_2 in the gas phase and v represents the superficial velocity, c_p represents the specific heat capacity of the bed material and ρ represents density of the bed material. Simulated frost front velocities were calculated from equation 6:

$$U_{frost} = \frac{Q_g}{A \rho c_p dT} \tag{6}$$

where U_{frost} is the frost front velocity, Q_g is the cooling duty required by the gas phase, A is the cross-sectional area of the capture column and dT is the temperature change. Table 1 compares simulated results
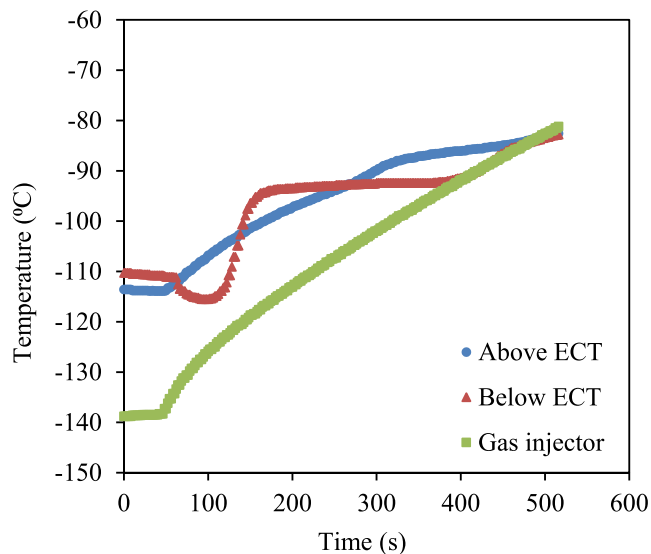
Table 1
Frost front velocity comparison.

Simulated results	Frost front velocity (mm/s)
This paper	1.12
Tuinier et al. [14]	1.33

produced for conditions in this paper and for experimental conditions from Tuinier et al.'s experimental work, which differ slightly by 18 %. One modification was made to Tunier et al's work before applying the correction factors which was to alter the starting temperature of the bed to match this work.

The reason the temperature profile above the ECT sensor does not show an obvious plateau was likely due to the ECT sensor. The ECT sensor attached to the capture column required the removal of insulation around the capture column, this caused the temperature of the bed material to be slightly higher than what the capture column can usually achieve. Applying the insulation around the ECT sensor affected the sensor's readings by increasing the effect of random artefacts that in the reconstructed images.

The ECT measurement procedure began when the capture stage was started by feeding a mixed gas of CO_2 and nitrogen through the mixed gas injector. Fig. 6 show that the ECT capacitance has little change during the entire CO_2 frost capture progress. In contrast, the presence of the temperature plateau in the temperature profiles in Fig. 5 shows that CO_2 frost is forming on the bed material. Based on the experimental results, we concluded that the designed ECT sensor and proposed image reconstruction methods could not properly estimate the permittivity change within the packed column in CO_2 frost capture progress.

The experimental rig fed through a gas mixture containing 18 % v/v CO_2 could not be detected by the ECT sensor. Increasing the concentration of CO_2 in the gas mixture would increase the mass of frost being deposited on the bed material which may have been detectable by the sensor; however, the experimental rig designed to feed up to 20 % CO_2 would not be able to accurately measure the concentration of the gas mixture and would risk desublimation of CO_2 frost within the liquid nitrogen precooler. Since detecting CO_2 frost at lower concentrations would be more difficult for the ECT sensor to detect, sensitivity analysis of the CO_2 frost experiments was not continued.

The tomography sensor could not accurately detect CO_2 frost growth on the surface of the bed material. This could be due to the relative permittivity of CO_2 in the solid and vapour phase as well as the ceramic bed material or the set up of the experiment is ineffective. Further experiments were conducted to determine whether the tomography sensor is able to detect frost growth of water droplets, which would show a much larger change in relative permittvity from phase change compared to CO_2.

3.2. Wet packing frosting experiment

Since the ECT sensor could not effectively detect CO_2 frost, the experimental procedure was changed to use water frost to explore the gas dynamic during ice frost formation progress in the packed column. The purpose of these experiments was to investigate two factors: firstly, whether the ECT sensor would detect water frost and subsequently whether tomography sensors were suitable for use with the experimental rig; and secondly, whether the freezing of water on the surface of the bed material gave any indication on the flow of gas through the capture column. If the ECT sensor detects water frost across the entire cross section of the capture column equally then that is evidence that the flow of gas through the capture column is uniform and predictable. Water was used as a replacement for CO_2 frost as the change in relative permittivity from water to ice (from 80 to 3.2) was substantially larger than from CO_2 gas to frost (from 1 to 1.6). Water relative permittivity is 88 at 0 °C and drops with rising temperature, e.g. to 55.3 at 100 °C. However, water (ice) relative permittivity is about 3.2 at -2 °C. The

Fig. 5. Temperature profiles of thermocouples above ECT, below ECT and gas injector under 40 LPM 18% v/v CO_2.
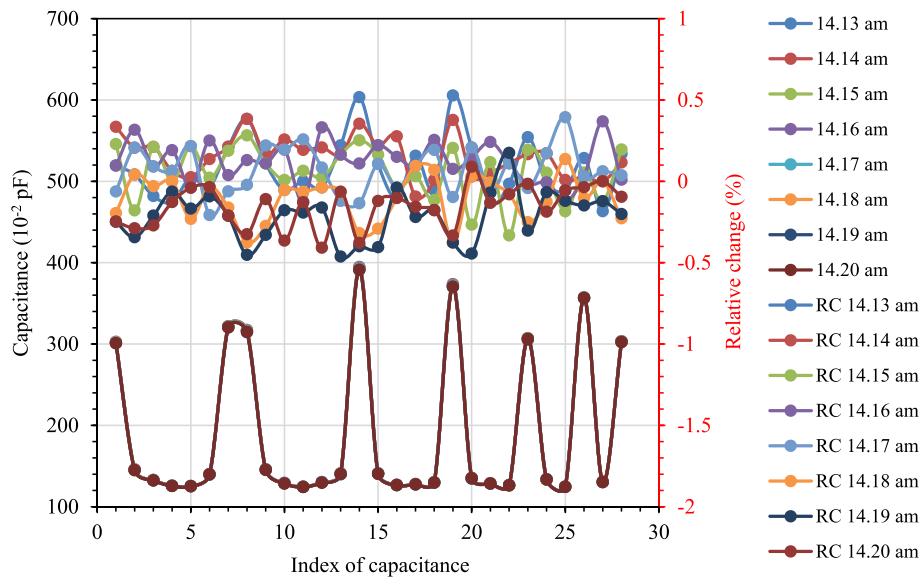
Fig. 6. ECT profiles for ceramic bed during CO_2 frost formation progress (RC: relative change of capacitance).

relative permittivity of the PTFE pipe is approximately 2.1. First, the ceramic bed material was wetted with water before being fed into the capture column, as the water would otherwise freeze inside the gas pipes when passing through the liquid nitrogen bath. Then cooling nitrogen gas was fed into the column at −15 ℃ to freeze the water present in the capture column. The nitrogen gas fed into the mixed gas line was used as the cooling gas for water related experiments, in order to simulate the mechanism of frost formation between the mixed gas and the bed material. The flow of cold gas through the column of wetted bed material caused the water to freeze. Thus, observing the freezing of water through the ECT showed the general flow pattern of cold gas through the bed material.

Fig. 7 shows the temperature profiles for the water frost and ceramic bed material experiments under different cooling gas flow rates. The gas injector's temperature profile mostly fluctuates within the range of −10 ℃ to −20 ℃. Keeping the temperature of the cooling gas stable proved to be more difficult due to the high cooling duty the liquid N_2 supplies to the cooling gas.

The temperature profile below the ECT sensor is dependent on the flow rate of gas. The temperature profile reaches 0 ℃ at roughly 250 s and −10 ℃ at 400 s for the 100 LPM graph (Fig. 7b), whereas the temperature profile reaches 0 ℃ at 500 s and −10 ℃ at 1000 s for the 50 LPM graph (Fig. 7a). The temperature profiles above the ECT sensor still have difficulty reaching the freezing temperature of the water. Due to the water being present on the bed material, the cooling duty must be

supplied by the cooling gas. The ceramic bed material density and the water are far higher than the cooling nitrogen gas. As a result, the poor cooling duty supplied by the gas phase slows down the cooling of the bed material.

Unexpectedly, the temperature profiles do not show a temperature plateau at 0 ℃. The reason for this is not entirely known. The most likely reason for the lack of a temperature plateau is that the ceramic bed material is wetted before being added to the capture column, which means there is minimal water present on the thermocouples during the experimental runs. Whereas in CO_2 frost experiments, the CO_2 frost desublimes out of the gas phase onto the bed material and likely desublimes onto the thermocouples as well. With no water freezing on the thermocouples, no temperature plateau is measured. The ECT sensors record a significant change in relative permittivity of the capture column, which indicates that water is freezing inside the capture column. Furthermore, samples of bed material taken from the capture column after the capture step showed frost present on the bed material.

Fig. 8 shows the ECT profiles for the water frost and ceramic bed material experiments during the water ice forming progress. Due to the different physical properties of water and CO_2, ECT for the wet packing frosting experiments needs to be calibrated separately. Based on the temperature profile, the temperature below ECT is 0 ℃ at approximately 4 mins. Two minutes later, the ECT capacitance reaches a peak value and this point is used as high calibration in the image reconstruction. A few minutes later, capacitance is keeping stable, and those points are used as
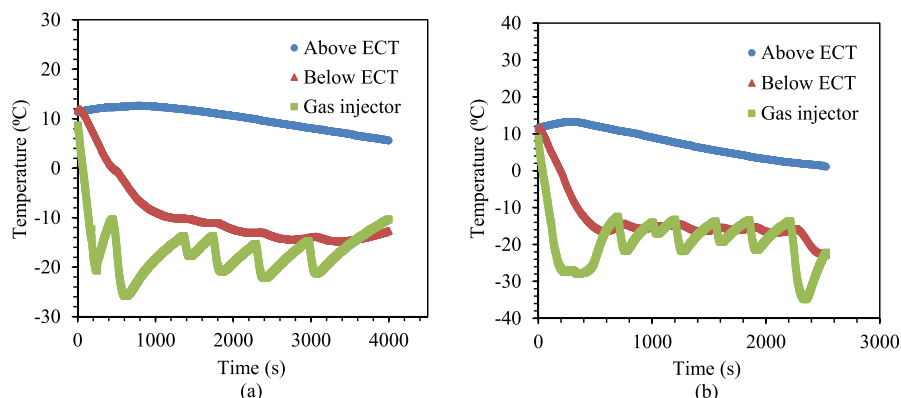
Fig. 7. Temperature profiles of thermocouples above ECT, below ECT and gas injector under (a) 50 LPM (b) 100 LPM (100% N_2).
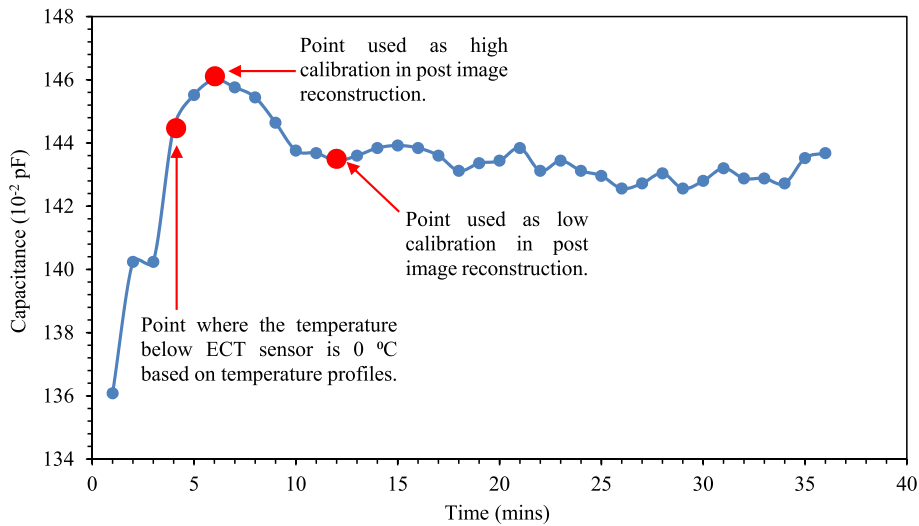
Fig. 8. ECT profiles for ceramic bed and water frost experiments.

low calibration in the image reconstruction. The calibration measurements are not made instantaneously, rather they are averaged over 60 s at a rate of 714 frames per second. This curve is consistent with the change of water relative permittivity with temperature. The reconstructed imaging therefore is expected to gradually change in permittivity distribution as high relative permittivity material (water) is frosting to low relative permittivity mater (ice).

3.3. Real-time measurement of frost distribution

In this section, dynamic imaging on ceramic packing cooling and water wetted ceramic packing frosting progress was carried out to validate the performance of the designed sensor. In ECT analysis, the capacitance change is used as an indicator to infer the frost formation in the packed column. Fig. 9 shows the reconstructed permittivity images for the experimental time sequence of frost development after the ceramic beads are wetted. The colour map of the reconstructed images is set to the same scale to facilitate the comparison. Two end and single end calibration methods used have been already described in Section 2.1.

In Fig. 9, the processes in the bed over time is reconstructed in real-time with two calibration methods. The overall trend of the two calibration methods is the same. While for the two end calibration method, the full calibration with high permittivity media $C_{H(j)}$ is inconvenient to

acquire as it would require the packed bed to be completely filled with water. Therefore, this calibration method can be less accurate as water only exists on the surface of ceramic packing during our experiment. Comparing the image in the single end calibration group and the double end calibration group shows that the high permittivity material (water) has the highest proportion at the beginning of frosting progress and the low permittivity material (ice) almost filled the column after a 10-minute treatment in the cooling gas.

The single end calibration method was chosen because it significantly reduces the error caused by inappropriate $C_{H(j)}$ required to reconstruct the image when compared to the two end calibration method and is therefore more suitable for a new technology to monitor real-time frost progress. According to Yang [30], the average E_{RMS} of the single end calibration method was 7.1 % compared with two end calibration method. The quantitative assessment in this work shows an acceptable decline in accuracy with the single end method using the values of low calibration data only, with $E_{RMS} \approx 5\%$ (using Equation (4)). In the single end calibration group results, a clear boundary of a circle shape can be identified in the centre area of the reconstructed images. Results on Fig. 9 show that the cooling progress has less effect on the permittivity located at the centre of the packed column. In the experimental data, liquid on the surface of ceramic beads causes the ECT capacitance to change from 0.41 % in the first minute to 2.96 % after ten
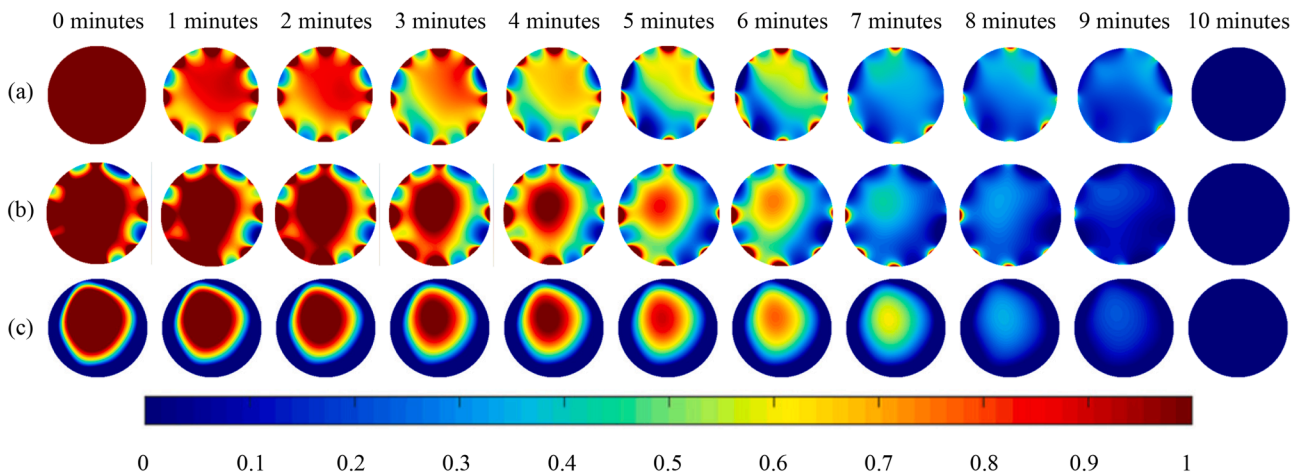
Fig. 9. Image reconstruction result of the wetted ceramic packing with (a) two end calibration method with Landweber algorithm (b) single end calibration method with Landweber algorithm (c) single end calibration method with MSBP algorithm from 0 min to 10 min.

minutes, which shows a clear effect of permittivity change during frost forming progress. A reasonable explanation for the result is that water has permittivity changes in a different form (liquid and solid). Prior to frost formation, the wetted ceramic beads with high permittivity are kept in the packed column. Later, the frost formed during the cooling results in the change of overall permittivity distribution after the frost appears. As a consequence, the permittivity within the packed column is decreased and the change of permittivity distribution is monitored by ECT. However, the reconstructed images in both methods have some red area close to the boundary of the image. The most likely explanation for those red dots is that there is considerably less water at the boundary close to the pipe wall than the centre area, so the frost formation permittivity change contributes significantly less at these areas. It has been proved that for cylindrical ECT sensors, the average spatial resolution greatly increases near the electrodes. Therefore, the teeth around the edges could be an artefact caused by ceramics beads as the whole cylindrical packing are filled up. Fig. 9 (c) shows the image reconstruction of the packed bed using the single end calibration method and MSBP algorithm [31]. In comparison with the two end calibration method result shown in Fig. 9 (a), the single end calibration method shows better reconstruction accuracy and better noise tolerance.

The reconstructed images show the phase of water in the bed material from liquid droplets to solid frost. The reconstructed images show that the colour change is roughly uniform across the cross-section of the capture column, and as previously mentioned, indicate that the gas flow through the pipe is relatively uniform. However, there appears to be some areas close to the wall which did not change in colour due to permittivity close to the wall not changing over time, this is most likely attributable to water not being present close to the wall due to the experimental set-up. The calibration method would therefore record no change at the wall.

It was found that in CO_2 frosting experiments shown in section 3.1, ECT results were affected by packing material selection. The results presented for water frost showed potential for the application of ECT to cryogenic carbon capture. But the high relative permittivity of the ceramic bed prevents the ECT sensor from detecting the small relative change in permittivity of CO_2 phase change. It would therefore be recommended in future work the selection of a bed material with a lower relative permittivity. It is anticipated that a packing material with lower permittivity, such as glass beads, should improve the detection of CO_2 frost. In addition, the preliminary model used in this work predicted that ceramic bed material with a high relative permittivity would see a large decrease in relative permittivity when CO_2 frost form on the surface. Complete coverage of CO_2 frost on the ceramic surface would affect the total permittivity of the ceramic material. It was expected that a bed material with high relative permittivity would show the greatest level of change in experiments. However, this has not been the case in the experiments, which could mean that CO_2 frost is not fully coating the bed material. The likely reasons for this are either that the bed material will have points of contact with each other to prevent frost completely surrounding each individual bead or that the frost nucleation and growth does not uniformly cover the surface of the bed material. Future modifications to the testing rig such as using a transparent column would help the observation of CO_2 frost formation phenomena. In order to perform sensitivity analyses, it is recommended to change more experimental conditions and variables to test their impact on frost distribution. Considering the low-temperature environment, the effect of change in temperature on the measurement capacitance must be recompensed.

4. Conclusion

In this study, the application of ECT for frost formation monitoring relevant to cryogenic carbon capture in a packed bed was investigated. Early experiments showed that the level of CO_2 frost formation was not readily detected using ECT, probably due to the large relative permittivity difference of the packed bed material and CO_2 frost. To validate the use of ECT in a packed bed under phase change conditions, experiments were conducted to substitute CO_2 for water, forming ice rather than CO_2 frost in the bed. An ECT sensor for frost imaging was applied and the single calibration method showed better performance. The experimental results with wetted ceramic packing showed that ECT could detect the progressive permittivity changes inside the packed column due to frost formation with a high temporal resolution. This demonstrates that with an improved experimental design, imaging of CO_2 frost formation on fixed packed beds could provide valuable information about deposition processes within the column.

Most notably, this is the first study to our best knowledge attempting to investigate CO_2 frost formation during cryogenic carbon capture with ECT. This study enables the potential ECT application to capture the instance change of frost distribution during cooling progress. However, this study only shows the preliminary results of water frost due to covid-19 restrictions that deterred further experiments, and the qualitative analysis is limited. Future studies should therefore focus on the quantitative analysis of the CO_2 frost formation during cryogenic carbon capture and data verification by proven techniques.

Data Availability

Information on the data supporting the results presented here, including how to access them, can be found at https://www2.bgs.ac.uk/ukccs/accessions/projects.html#item162545?projectID=20909612 , an open-source online data repository hosted at UKCCSRC Data and Information Archive [32].

CRediT authorship contribution statement

Yuan Chen: Formal analysis, Investigation, Methodology, Software, Data curation, Writing – original draft. **David Cann:** Formal analysis, Investigation, Methodology, Writing – original draft. **Jiabin Jia:** Supervision, Investigation, Conceptualization, Writing – review & editing. **Carolina Font-Palma:** Conceptualization, Supervision, Resources, Project administration, Funding acquisition, Writing – review & editing.

Declaration of Competing Interest

The authors declare that they have no known competing financial interests or personal relationships that could have appeared to influence the work reported in this paper.

Acknowledgements

References

[1] BP. BP Energy Outlook; 2020. Available from: https://www.bp.com/content/dam/bp/business-sites/en/global/corporate/pdfs/energy-economics/energy-outlook/bp-energy-outlook-2020.pdf.

[2] Tauseef Hassan S, Xia E, Lee C-C. Mitigation pathways impact of climate change and improving sustainable development: The roles of natural resources, income, and CO2 emission. Energy Environ 2021;32(2):338–63.

[3] Bui M, Adjiman CS, Bardow A, Anthony EJ, Boston A, Brown S, et al. Carbon capture and storage (CCS): the way forward. Energy Environ Sci 2018;11(5):1062–176.

[4] Osman AI, Hefny M, Abdel Maksoud MIA, Elgarahy AM, Rooney DW. Recent advances in carbon capture storage and utilisation technologies: a review. Environ Chem Lett 2021;19(2):797–849.

[5] Sreenivasulu B, Gayatri D, Sreedhar I, Raghavan K. A journey into the process and engineering aspects of carbon capture technologies. Renew Sustain Energy Rev 2015;41:1324–50.

[6] Lively RP, Chance RR, Koros WJ. Enabling low-cost CO2 capture via heat integration. Ind Eng Chem Res 2010;49(16):7550–62.

[7] Koytsoumpa EI, Bergins C, Kakaras E. The CO2 economy: Review of CO2 capture and reuse technologies. The Journal of supercritical fluids 2018;132:3–16.

[8] Tan L, Shariff A, Lau K, Bustam M. Factors affecting CO2 absorption efficiency in packed column: A review. J Ind Eng Chem 2012;18(6):1874–83.

[9] Song C, Liu Q, Deng S, Li H, Kitamura Y. Cryogenic-based CO2 capture technologies: State-of-the-art developments and current challenges. Renew Sustain Energy Rev 2019;101:265–78.

[10] Font-Palma C, Cann D, Udemu C. Review of Cryogenic Carbon Capture Innovations and Their Potential Applications. C 2021;7(3):58.

[11] Ali A, Maqsood K, Syahera N, Shariff AB, Ganguly S. Energy minimization in cryogenic packed beds during purification of natural gas with high CO2 content. Chem Eng Technol 2014;37(10):1675–85.

[12] Nasrifar K, Moshfeghian M. Prediction of carbon dioxide frost point for natural gas and LNG model systems. Journal of natural gas science and engineering 2020;76: 103206-.

[13] Song C-F, Kitamura Y, Li S-H, Jiang W-Z. Analysis of CO2 frost formation properties in cryogenic capture process. Int J Greenhouse Gas Control 2013;13: 26–33.

[14] Tuinier MJ, Sint Annaland vM, Kramer GJ, Kuipers JAM. Cryogenic CO2 capture using dynamically operated packed beds. Chemical engineering science 2010;65 (1):114-9.

[15] Tuinier MJ, van Sint AM, Kuipers JAM. A novel process for cryogenic CO2 capture using dynamically operated packed beds—An experimental and numerical study. Int J Greenhouse Gas Control 2011;5(4):694–701.

[16] Willson P, Lychnos G, Clements A, Michailos S, Font-Palma C, Diego ME, et al. Evaluation of the performance and economic viability of a novel low temperature carbon capture process. Int J Greenhouse Gas Control 2019;86:1–9.

[17] Cann D, Font-Palma C, Willson P. Experimental analysis of CO2 frost front behaviour in moving packed beds for cryogenic CO2 capture. Int J Greenh Gas Con 2021;107:103291.

[18] Babar M, Bustam MA, Ali A, Maulud AS, Shafiq U, Shariff AM, et al. Efficient CO2 capture using NH2–MIL–101/CA composite cryogenic packed bed column. Cryogenics (Guildford) 2019;101:79–88.

[19] Shchelkunov VN, Rudenko NZ, Shostak YV, Dolganin VI. Surface desublimation of carbon dioxide from binary gas mixtures. Journal of Engineering Physics 1986;51 (6):1432–5.

[20] Sun S, Zhang W, sun j, Cao Z, Xu L, Yan Y. Real-Time Imaging and Holdup Measurement of Carbon Dioxide Under CCS Conditions Using Electrical Capacitance Tomography. IEEE sensors journal 2018;18(18):7551–9.

[21] Shao D, Yan Y, Zhang W, Sun S, Sun C, Xu L. Dynamic measurement of gas volume fraction in a CO2 pipeline through capacitive sensing and data driven modelling. Int J Greenhouse Gas Control 2020;94:102950.

[22] Wu H, Buschle B, Yang Y, Tan C, Dong F, Jia J, et al. Liquid distribution and hold-up measurement in counter current flow packed column by electrical capacitance tomography. Chem Eng J 2018;353:519–32.

[23] Li Z, Chen Y, Yang Y, Liu C, Lucquiaud M, Jia J. Flow regime transition in countercurrent packed column monitored by ECT. Chemical engineering journal (Lausanne. Switzerland 1996;2021(420):129841.

[24] Xia T, Xie H, Wei A, Zhou R, Qiu L, Zhang X. Preliminary study on three-dimensional imaging of cryogenic two-phase flow based on electrical capacitance volume tomography. Cryogenics (Guildford) 2020;110:103127-.

[25] Isaksen Ø. A review of reconstruction techniques for capacitance tomography. Meas Sci Technol 1996;7(3):325.

[26] Wang H, Yang W. Scale-up of an electrical capacitance tomography sensor for imaging pharmaceutical fluidized beds and validation by computational fluid dynamics. Meas Sci Technol 2011;22(10):104015.

[27] Yang W, Peng L. Image reconstruction algorithms for electrical capacitance tomography. Meas Sci Technol 2002;14(1):R1.

[28] Yang Y, Peng L, Jia J. A novel multi-electrode sensing strategy for electrical capacitance tomography with ultra-low dynamic range. Flow Meas Instrum 2017; 53:67–79.

[29] Span R, Wagner W. A new equation of state for carbon dioxide covering the fluid region from the triple-point temperature to 1100 K at pressures up to 800 MPa. J Phys Chem Ref Data 1996;25(6):1509–96.

[30] Yang W. Calibration of capacitance tomography systems: a new method for setting system measurement range. Meas Sci Technol 1996;7(6):L863.

[31] Jia J, Wang M, Faraj Y. Evaluation of EIT systems and algorithms for handling full void fraction range in two-phase flow measurement. Meas Sci Technol 2014;26(1): 015305.

[32] Font-Palma C, Jia J, Chen Y, Cann D. UKCCSRC 2020: Electrical Capacitance Tomography and Temperature profiles data for the experiment of CO2 frost formation during cryogenic carbon capture with tomography analysis at The University of Chester, 2020, UKCCSRC Data and Information Archive, https://www2.bgs.ac.uk/ukccs/accessions/projects.html#item162545? projectID=20909612.